

Efficient Feature Aggregation and Scale-Aware Regression for Monocular 3D Object Detection

Yifan Wang, Xiaochen Yang, Fanqi Pu,
Qingmin Liao, *Senior Member, IEEE*, and Wenming Yang, *Senior Member, IEEE*

Abstract—Monocular 3D object detection has attracted great attention due to simplicity and low cost. Existing methods typically follow conventional 2D detection paradigms, first locating object centers and then predicting 3D attributes via neighboring features. However, these methods predominantly rely on progressive cross-scale feature aggregation and focus solely on local information, which may result in a lack of global awareness and the omission of small-scale objects. In addition, due to large variation in object scales across different scenes and depths, inaccurate receptive fields often lead to background noise and degraded feature representation. To address these issues, we introduce MonoASRH, a novel monocular 3D detection framework composed of Efficient Hybrid Feature Aggregation Module (EH-FAM) and Adaptive Scale-Aware 3D Regression Head (ASRH). Specifically, EH-FAM employs multi-head attention with a global receptive field to extract semantic features for small-scale objects and leverages lightweight convolutional modules to efficiently aggregate visual features across different scales. The ASRH encodes 2D bounding box dimensions and then fuses scale features with the semantic features aggregated by EH-FAM through a scale-semantic feature fusion module. The scale-semantic feature fusion module guides ASRH in learning dynamic receptive field offsets, incorporating scale priors into 3D position prediction for better scale-awareness. Extensive experiments on the KITTI and Waymo datasets demonstrate that MonoASRH achieves state-of-the-art performance.

Index Terms—3D object detection, monocular, scale-aware, scene understanding, autonomous driving.

I. INTRODUCTION

IN RECENT years, 3D object detection has emerged as a pivotal area of research, particularly driven by its critical role in autonomous systems, robotics, and augmented reality. The ability to accurately detect and localize objects in three-dimensional space is essential for applications that require a high degree of spatial awareness, especially for autonomous driving systems [1], [2].

Advancements in sensors such as LiDAR, radar, and stereo cameras have enhanced 3D object detection with point cloud data, radar signals, and depth maps. However, LiDAR’s high-resolution point clouds [3], [4], [5], [6] and stereo methods’ depth maps [7], [8] require additional calibration. CAD [9], [10] and multi-frame [11] approaches improve shape and movement tracking but are also computationally intensive.

Yifan Wang, Fanqi Pu, Qingmin Liao, and Wenming Yang are with the Department of Electronic Engineering, Shenzhen International Graduate School, Tsinghua University, Shenzhen 518055, China (e-mail: yf-wang23@mails.tsinghua.edu.cn; pfq23@mails.tsinghua.edu.cn; liaoqm@tsinghua.edu.cn; yang.wenming@sz.tsinghua.edu.cn).

Xiaochen Yang is with the School of Mathematics and Statistics, University of Glasgow, Glasgow, G12 8QQ, UK (e-mail: xiaochen.yang@glasgow.ac.uk).

Compared to the above methods, monocular vision systems offer a more cost-effective and deployable solution, though they struggle with accurately extracting 3D information from 2D images due to the absence of direct depth perception.

Therefore, current advancements in monocular 3D detection have focused on improving depth estimation accuracy. Methods like [12], [13], [14], [15], [16], [17] following the CenterNet [18] paradigm, use direct regression to estimate the 3D center depth of the target object. [9], [19], [20], [21], [22] incorporates geometric constraints into depth estimation to enhance target depth recovery. [23], [24], [25], [26], [27] effectively integrate geometric depth with regressed depth, improving the network’s generalization ability. However, these approaches often decouple 2D and 3D feature regression, predicting 2D attributes (x, y, w, h) and 3D attributes (x, y, z, w, h, l, yaw) independently. This separation overlooks the potential relationship between 2D priors and the 3D position of objects. Briefly, distant objects often occupy small areas in images, while nearby objects dominate, leading to challenges in extracting relevant features using fixed receptive fields. This issue is evident in the contrast between the attention heatmaps of the networks shown in Fig. 1. It can be seen that DEVIANT [22] and MonoLSS [17] struggle to focus on smaller, distant objects, particularly in the pedestrian category. Moreover, DEVIANT [22] tends to inadvertently attend to irrelevant background noise. Some previous works attempted to address this issue. Chen et al. proposed a shape-aware auxiliary training task [28]. [29] integrated deformable convolutions [30] to enhance the model’s adaptability to features. Although these methods achieve dynamic receptive field adjustment to some extent, they have not explicitly considered object scale within a scene, nor dynamically adjusted the model’s attention based on different scales.

To address the aforementioned limitations, this paper proposes the novel Efficient Hybrid Feature Aggregation Module (EH-FAM) and Adaptive Scale-Aware 3D Regression Head (ASRH). Inspired by RT-DETR’s [31] success in 2D detection, EH-FAM integrates Vision Transformers with CNNs to efficiently aggregate visual features, significantly reducing model complexity compared to traditional methods like DLAUp [32]. The EH-FAM employs self-attention based within-scale feature interactions on the highest-level features, effectively capturing the semantic information of small-scale objects. Convolutional operations are then utilized for feature fusion, providing a more fine-grained cross-scale feature representation. Subsequently, ASRH encodes 2D bounding box dimensions to capture scale features, which are fused

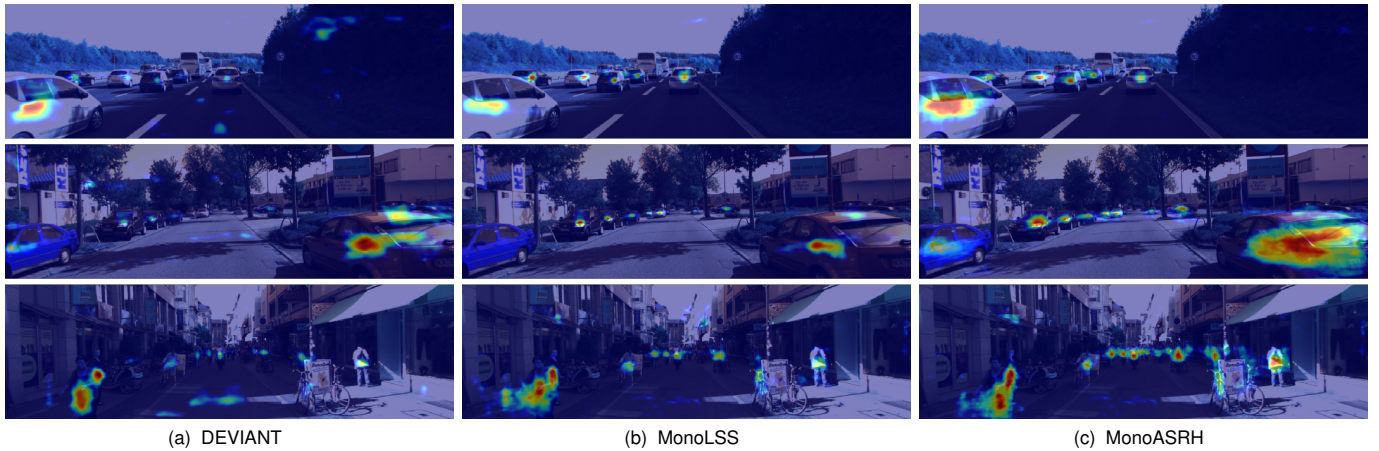


Fig. 1. Visualization of attention heatmaps for different models: (a) DEVIANT [22], (b) MonoLSS [17], and (c) Our proposed MonoASRH. Previous methods struggle to effectively capture distant and occluded objects due to fixed receptive fields. In contrast, our MonoASRH overcomes these limitations by dynamically adjusting attention based on different scales, including for the car vs. pedestrian category.

with semantic features extracted from the cross-scale feature through a specially designed scale-semantic feature fusion module. The fused features guide the learning of receptive field offsets, which are then applied to deformable convolutions, enhancing the model’s ability to adapt to varying object scales. Furthermore, ASRH utilizes a spatial variance-based attention mechanism to adaptively differentiate foreground objects from noise within semantic features. Additionally, we introduce the Selective Confidence-Guided Heatmap Loss to facilitate ASRH to prioritize high confidence detections and mitigates the impact of hard samples.

Our contributions can be summarized as follows:

- We introduce a plug-and-play module called Efficient Hybrid Feature Aggregation Module, which is designed for efficient cross-scale feature aggregation.
- We propose a novel Adaptive Scale-Aware 3D Regression Head, which dynamically adjusts the network’s receptive field according to object scale. By leveraging 2D prior information, ASRH facilitates 3D bounding box regression.
- Extensive experiments on the KITTI 3D object detection benchmark [33] and Waymo Open dataset [34] show that our MonoASRH achieves better results compared to previous state-of-the-art methods.

II. RELATED WORKS

Monocular 3D object detection aims to estimate the 3D attributes of objects from a single image. In this section, we summarize the previous monocular 3D object detection algorithms. Broadly speaking, these methods can be categorized into three main approaches: depth map-based, center-based, and transformer-based methods.

A. Depth Map-Based Methods

Depth map-based methods [35] aim to compensate for the lack of spatial depth information in monocular vision by leveraging independent depth estimation networks to regress depth maps from monocular images. These depth estimation

branches are typically trained under supervision using ground truth depth maps [36], [37] or through self-supervised learning with sequential images [38], [39]. [40] employs depth-guided convolutions to address scale variance issues, while [41] integrates multi-scale depth features with image features. [42] enhances these approaches by directly incorporating 3D coordinates into the input data. Additionally, other works [43], [44], [45] convert image-like depth maps into point-like pseudo-LiDAR representations to simulate LiDAR point clouds. Techniques such as [46] utilize external depth estimation networks like [47] to align 3D bounding boxes. Other methods [48] incorporate disparity prediction modules within dual-network structures to generate 2D region proposals and predict 3D attributes, though they have been criticized for potential performance bias. Subsequent models like [49] and [44] improve depth accuracy and integrate RGB features to enhance 3D localization.

However, these approaches often lack 3D confidence estimation components [50], limiting their performance. Furthermore, reliance on pre-trained depth estimation networks, optimized for pixel-level accuracy rather than 3D detection, poses challenges in accurately determining the depth of foreground objects. Recent studies [51] have also highlighted issues of biased results due to overlap between training and validation datasets, complicating the effectiveness of depth map-based methods in monocular 3D detection.

B. Center-Based Methods

Many center-based methods [21], [25], [52], [53], [54], [55] are extensions of the popular anchor-free CenterNet [18] approach, which simplifies the detection process and improves efficiency by mapping various 3D bounding box attributes to a single center point. [13] inherits this center-based framework and eliminates the need for estimating 2D bounding boxes. [14] identifies depth error as the primary factor limiting the accuracy of monocular 3D object detection. [16] enhances network generalization by introducing auxiliary learning tasks. Meanwhile, [14], [20], [22] incorporate geometric constraints

into depth estimation on top of regressed depth, with [14] further proposing a Hierarchical Task Learning strategy to ensure more stable training. [24] leverages multiple depth attributes, combining them to generate various depth estimates, which are then optimally weighted through multi-task learning [56]. [57] utilizes a loss function called Homography Loss to balance the positional relationship between different objects. [27] introduces the concept of complementary depth, utilizing geometric relationships between multiple depth cues to achieve formal complementarity. [28], [58] propose shape-aware schemes and plane-constrained 3D detection frameworks, respectively, to address occlusion issues in monocular vision. In [59], the proposed framework addresses the issue of over-regularization in monocular 3D object detection by gradually relaxing regularization constraints. [17] proposes a novel Learnable Sample Selection module, using Gumbel-Softmax probabilistic sampling [60] to distinguish between positive and negative samples in depth maps, effectively reducing interference from irrelevant foreground and background information. Although center-based methods offer many advantages, they tend to overlook the guidance provided by 2D prior information in regressing 3D detection attributes. As a result, the network may neglect the distance and size of the detected object when predicting its 3D properties.

C. Transformer-Based Methods

Recently, end-to-end transformer-based detectors (DETRs) [61], [62], [63] have achieved remarkable success in 2D object detection. Subsequently, several works have extended Transformer-based detection frameworks to monocular 3D object detection, enhancing the model’s global perception capabilities. [64] uses transformer to achieve end-to-end 3D bounding box prediction by projecting learnable 3D queries in 2D images. [5] leverages LiDAR for auxiliary supervision, injecting global depth information into the Transformer to guide detection. On the other hand, [65] fully interacts with depth and visual features through a depth cross-attention layer in the decoder, without relying on any additional data. To improve inference efficiency, [66] introduces an adaptive token Transformer, allowing more refined tokens to be allocated to the more critical regions of the image. However, the introduction of a global receptive field inevitably causes these networks to focus on background noise, leading to slow and unstable training convergence. Moreover, the high computational complexity and slow inference speed of Transformer-based monocular 3D detectors make them less suitable for deployment in real-time autonomous driving systems.

III. PROPOSED METHODOLOGY

In this section, we introduce our MonoASRH architecture. The overall framework, shown in Fig. 2, mainly consists of backbone, Efficient Hybrid Feature Aggregation Module, 2D regression head, and Adaptive Scale-Aware 3D Regression Head. Our pipeline mainly builds on the GUPNet [21]. Detailed implementation will be discussed later in this section.

A. Overall Architecture

For a given RGB image $I \in \mathbb{R}^{H \times W \times 3}$, we extract multi-scale deep features using a pre-trained DLA-34 backbone [32]. These features, represented as $\{S_1, S_2, S_3, S_4\}$, undergo further refinement and cross-scale fusion through the proposed EH-FAM. The resulting aggregated features are denoted as $F \in \mathbb{R}^{\frac{H}{4} \times \frac{W}{4} \times C}$. Similar to [21], our 2D detector is based on CenterNet [18]. We feed the deep features F into three 2D detection heads to regress heatmaps $H \in \mathbb{R}^{\frac{H}{4} \times \frac{W}{4} \times 3}$, 2D offsets $O_{2D} \in \mathbb{R}^{\frac{H}{4} \times \frac{W}{4} \times 2}$, and 2D sizes $S_{2D} \in \mathbb{R}^{\frac{H}{4} \times \frac{W}{4} \times 2}$, enabling the prediction of 2D object centers and dimensions.

The deep features F are also fed into ASRH for 3D attributes prediction. Specifically, RoI-Align extracts local semantic features $F_R \in \mathbb{R}^{n \times d \times d \times C}$ from F based on 2D boxes, where $d \times d$ is the RoI-Align size and n is the number of regions of interest. Subsequently, we denote the size of 2D bounding box corresponding to each region of interest as $S_R \in \mathbb{R}^{n \times 2}$, which is further encoded into scale features. Scale features and semantic features are then fused through the scale-semantic feature fusion module. Ultimately, ASRH outputs 3D bounding box sizes $S_{3D} \in \mathbb{R}^{n \times 3}$, 3D center offsets $O_{3D} \in \mathbb{R}^{n \times 2}$, yaw angle $\Theta \in \mathbb{R}^{n \times 24}$, direct depth $D \in \mathbb{R}^{n \times d \times d}$, and depth uncertainty $D_U \in \mathbb{R}^{n \times d \times d}$. Additionally, a depth attention map $D_M \in \mathbb{R}^{n \times d \times d}$ is employed to reduce the impact of irrelevant information, improving 3D detection accuracy.

B. Efficient Hybrid Feature Aggregation Module

To efficiently aggregate features extracted by backbone at different scales into deep representations, we propose EH-FAM, a plug-and-play cross-scale feature aggregator. The “hybrid” module combines attention-based intra-scale interactions with CNN-based cross-scale fusion for improved performance and computational efficiency. The detailed implementation of EH-FAM is shown in Fig. 3.

1) *Self-Attention Block*: The EH-FAM receives four feature maps with different downsampling ratios as input. To ensure global extraction of rich semantic information about small-scale objects, we apply multi-head self-attention to the highest-level feature S_4 . We use separate linear projections for queries, keys, and values:

$$Q_i = (X_{seq} + P_e) W_i^{(Q)}, \quad K_i = (X_{seq} + P_e) W_i^{(K)}, \quad (1)$$

$$V_i = X_{seq} W_i^{(V)}, \quad (2)$$

where $X_{seq} \in \mathbb{R}^{T \times C}$ obtained by flattening S_4 , $T = \frac{H}{32} \times \frac{W}{32}$ represents sequence length, P_e is the positional embedding vector, and $W_i^{(Q)}, W_i^{(K)}, W_i^{(V)}$ are the query, key, and value transformation matrices for the i -th head, respectively. For each head, the attention output is a weighted sum of the values:

$$Z_i = \text{Softmax} \left(\frac{Q_i K_i^T}{\sqrt{C}} \right) V_i. \quad (3)$$

Finally, the concatenated output is passed through a linear layer to combine the multiple heads into a single output:

$$Z_{out} = [Z_1, Z_2, \dots, Z_h] W_o, \quad (4)$$

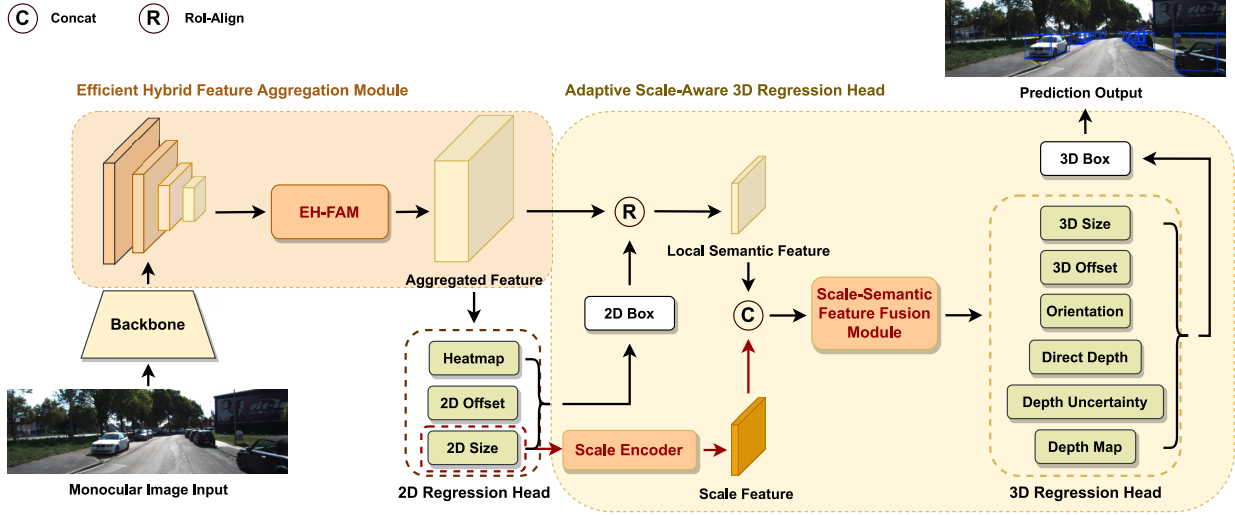


Fig. 2. Overview of our framework. The Efficient Hybrid Feature Aggregation Module (EH-FAM) efficiently aggregates multi-scale features. The Adaptive Scale-Aware 3D Regression Head (ASRH) fuses scale features with local semantics to guide the learning of 3D regression head.

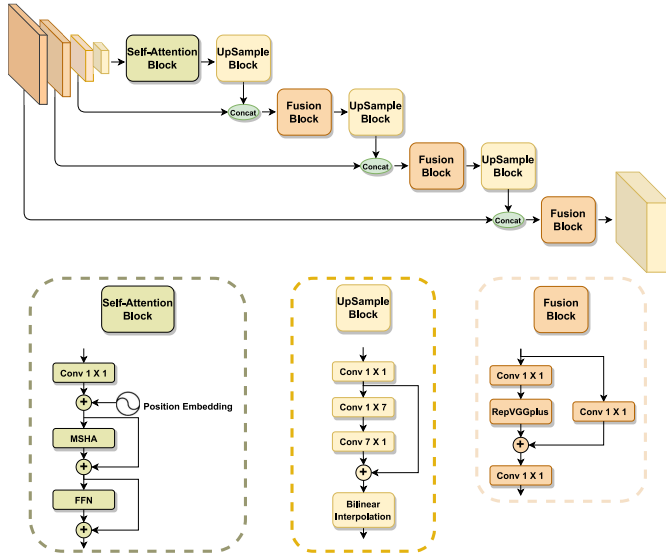


Fig. 3. Efficient Hybrid Feature Aggregation Module. Self-attention is applied only to the highest-level semantic feature map using an 8-head multi-head attention mechanism. Besides, all convolutional layers use the Mish activation function for improved feature representation.

where $W_o \in \mathbb{R}^{(h \times d_v) \times C}$ is a learnable projection matrix. h and d_v denote the number of attention heads and the channel dimensions of V_i , respectively. Next, the output of the multi-head attention is passed through an FFN and then reshaped back to its original spatial dimensions, denoted as S_{out} .

2) *Upsampling Block*: To improve EH-FAM’s ability to perceive small-scale objects, we design an upsample block and fusion block composed of lightweight convolutional modules. These blocks enable cross-scale information interaction and enhance the extraction of local semantic features. In the upsample block, we replace DLAUp’s [32] large-kernel transposed convolutions with bilinear upsampling. To further mitigate information loss, we apply a 7×7 convolution prior to upsampling, which effectively refines feature maps. For efficiency, we decouple the 7×7 convolution into successive

1×7 and 7×1 convolutions, following the approach in [67]. Additionally, since some categories, such as Pedestrian and Cyclist, have relatively large aspect ratios but small sizes, decoupled convolutions in the horizontal and vertical directions are adopted to capture these elongated scale features.

3) *Fusion Block*: In the fusion block, we employ the RepVGGplus block [68], which leverages re-parameterization techniques to convert a multi-branch ResNet-style architecture into a single-path VGG-like model during inference. This maintains the representational power of the model while accelerating inference. The final deep features are aggregated as follows:

$$F = f(S_{out}, S_3, S_2, S_1), \quad (5)$$

where f denotes the upsampling and cross-scale fusion operations.

C. Adaptive Scale-Aware 3D Regression Head

As illustrated in Fig. 4, the proposed Adaptive Scale-Aware 3D Regression Head decomposes the 3D bounding box regression process into three stages. First, scale features are captured by encoding the 2D bounding box dimensions. Next, a scale-semantic fusion module combines these scale features with semantic features extracted from the region of interest, dynamically adjusting the 3D regression head’s receptive field. Given the limited image space occupied by foreground objects (e.g., the car class in KITTI covers just 11.42% of depth pixels), we also introduce an attention mask to ensure the 3D regression head focuses on relevant foreground regions. Finally, the 3D regression head outputs the 3D bounding box attributes.

1) *Scale Encoder*: The Scale Encoder uses MLP to transform 2D geometric properties into a high-dimensional representation. By learning this transformation, the Scale Encoder effectively encodes scale information. For each region of

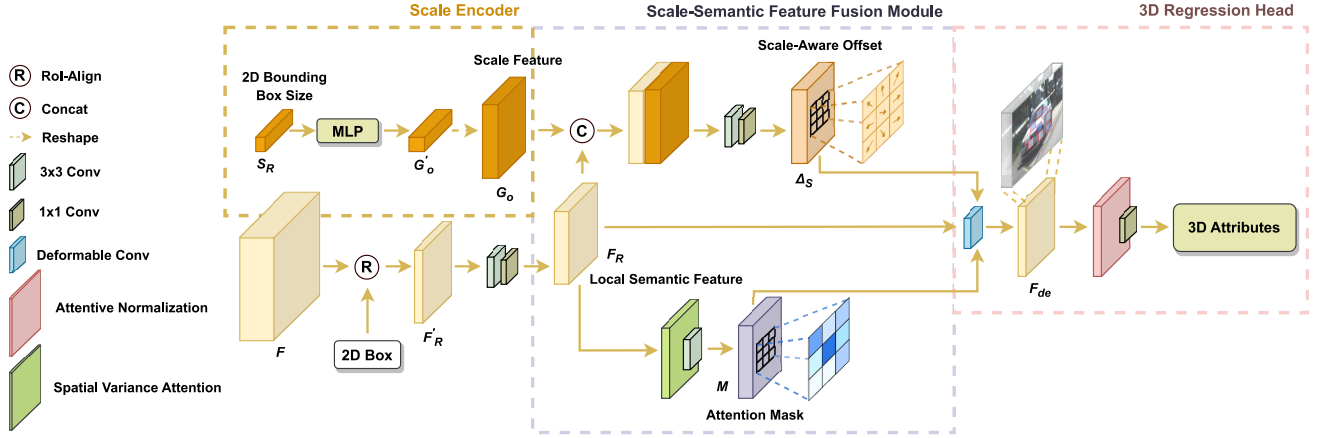


Fig. 4. The proposed Adaptive Scale-Aware 3D Regression Head. In Scale-Aware Offset, brown arrows indicate the direction of dynamic adjustment of the convolutional receptive field. In Attention Mask, varying shades of blue represent different weights at each position in the convolution kernel. Our network includes six parallel 3D regression heads of this structure to regress different 3D attributes.

interest, the corresponding 2D bounding box size $S_R \in \mathbb{R}^{n \times 2}$ is mapped to a high-dimensional feature space:

$$G'_o = \text{MLP}(S_R), \quad (6)$$

where $G'_o \in \mathbb{R}^{n \times 32}$. Simultaneously, we apply a series of convolutional layers to further refine the feature maps F'_R within the region of interest, obtaining the local semantic features F_R :

$$F_R = \text{Conv}(\text{ReLU}(\text{Conv}(F'_R))), \quad (7)$$

where $F_R \in \mathbb{R}^{n \times d \times d \times C}$, $d \times d$ is the RoI-Align size. Offset G'_o is then reshaped to match the spatial dimensions of the F_R , denoted as G_o .

2) *Scale-Semantic Feature Fusion Module*: This module comprises two key components: offset feature generation and attention mask generation. For offset generation, the scale feature G_o and local semantic features F_R are concatenated. The combined features are processed through a stacked convolutional layer consisting of 3×3 and 1×1 convolutions, producing a scale-aware offset Δ_S , which is used to dynamically adjust the receptive field in subsequent deformable convolutions.

$$\Delta_S = \text{Conv}(\text{ReLU}(\text{Conv}([G_o, F_R]))), \quad (8)$$

where $\Delta_S \in \mathbb{R}^{n \times d \times d \times 18}$, and 18 represents the offset of each spatial position in the deformable convolution kernel.

In the attention mask generation component, inspired by [69], we design an attention mechanism based on spatial variance. This mechanism emphasizes regions with significant deviations from the mean, which are often foreground regions of interests. First, the mean of the local semantic features F_R are computed across spatial dimensions:

$$\mu(F_R) = \frac{1}{d \times d} \sum_{i=1}^d \sum_{j=1}^d F_R^{n,i,j,c}. \quad (9)$$

Then, we calculate the squared difference of each pixel relative to the mean across the spatial dimensions of the feature map:

$$V = \left(F_R^{n,i,j,c} - \mu(F_R) \right)^2. \quad (10)$$

Using the squared difference obtained from the Eqn. 10, the attention weights can be calculated as:

$$Y = \sigma \left(\frac{V}{\frac{1}{d \times d - 1} \sum_{i=1}^d \sum_{j=1}^d V_{i,j} + \lambda} + 0.5 \right), \quad (11)$$

where λ is a small positive constant. σ is a projection function implemented by convolution followed by sigmoid. Normalizing by the variance provides a measure of how relatively important a specific deviation is compared to the overall distribution of deviations.

Finally, a convolutional layer with a sigmoid activation function is applied to generate the mask:

$$M = \sigma(F_R \circ Y), \quad (12)$$

where $M \in \mathbb{R}^{n \times d \times d \times 9}$, and \circ denotes element-wise multiplication.

3) *3D Regression Head*: To achieve scale-aware dynamic receptive field adjustment, the first layer of the 3D regression head utilizes deformable convolutions [30]. As shown in Eqn. 13, the offset Δ_S and attention mask M generated by the Scale-Semantic Feature Fusion Module are applied to this layer, allowing the model to better detect and localize objects of varying scales:

$$F_{de} = \sum_{P_n \in \Omega} M_{P_n} \cdot W_{P_n} \cdot F_R \left(\Delta_S^{P_n} + P_n \right), \quad (13)$$

where Ω represents the local neighborhood for a 3×3 kernel, P_n enumerates the locations in Ω , $\Delta_S^{P_n}$ is the learned offset for each position in the convolution kernel, W_{P_n} is the weight of the convolution kernel at position P_n , and M_{P_n} controls the contribution of the corresponding kernel position.

Next, we normalize the feature map F_{de} using the Attentive Normalization layer [70], which is a light weight module integrating feature normalization and channel-wise feature attention:

$$F_n = \text{AN}(F_{de}). \quad (14)$$

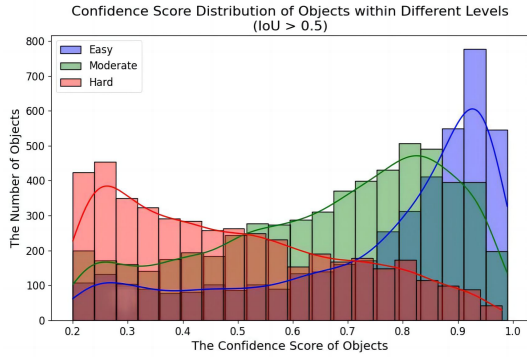


Fig. 5. We visualize the confidence score distribution of MonoASRH across three difficulty levels in the KITTI dataset, considering only samples with a 3D IoU greater than 0.5. The model tends to assign higher confidence scores to easy samples, while showing lower confidence for hard samples.

Due to AN’s mixture modeling approach to affine transformation, which recalibrates features after standardization, it is employed in the regression head to facilitate the learning of more expressive latent feature representations. Finally, the feature map is processed through a LeakyReLU activation function and a 1×1 convolution for channel mapping, ultimately regressing the 3D bounding box attributes.

D. Loss Function

1) *Selective Confidence-Guided Heatmap Loss*: Easy samples, which are typically fully visible and closer to the camera, exhibit less scale complexity. As a result, our scale-aware mechanism struggles to provide additional focus on these targets. To address this issue, we propose the Selective Confidence-Guided Heatmap Loss, which encourages the model to focus more on high-confidence samples, given that the network tends to assign higher confidence scores to easy samples (as shown in Fig. 5). Specifically, this loss function uses an improved version of Focal Loss [71] as the primary loss and introduces a Selective Confidence-Guided (SCG) Loss as an auxiliary loss (Eqn. 15) to enhance training.

$$\mathcal{L}_{SCG} = -\frac{1}{B} \sum_{i=1}^B \sum_{j=1}^K \begin{cases} \log(t_{ij}), & t_{ij} > T \\ 0, & \text{otherwise} \end{cases}, \quad (15)$$

where B is the batch size, K is the maximum number of detectable objects per image, t_{ij} are the top K points with the highest confidence in the predicted heatmap, and T is the confidence threshold.

The focal loss introduces a dynamic weighting for heatmap regression. The SCG Loss encourages the ASRH to prioritize high-confidence samples, which is critical for accurate detection of closer objects. Meanwhile, optimizing for high-confidence objects can to some extent mitigate the overfitting of noise in low-confidence samples. The final heatmap regression loss is a weighted combination of these two losses:

$$\mathcal{L}_{Heatmap} = \mathcal{L}_{focal} + \lambda \mathcal{L}_{SCG}. \quad (16)$$

In the experiment, T was taken as 0.9 and λ as 0.01.

2) *Total Loss*: The overall network loss \mathcal{L} consists of two components: 2D object loss \mathcal{L}_{2D} and 3D object loss \mathcal{L}_{3D} . Mathematically, the composite loss function is expressed as:

$$\mathcal{L} = \mathcal{L}_{2D} + \mathcal{L}_{3D}. \quad (17)$$

The 2D object loss follows the design of CenterNet [18]. It includes the Selective Confidence-Guided Heatmap Loss $\mathcal{L}_{Heatmap}$, 2D center offset loss $\mathcal{L}_{O_{2D}}$ and 2D size loss $\mathcal{L}_{S_{2D}}$:

$$\mathcal{L}_{2D} = \mathcal{L}_{Heatmap} + \mathcal{L}_{O_{2D}} + \mathcal{L}_{S_{2D}}, \quad (18)$$

where $\mathcal{L}_{O_{2D}}$ and $\mathcal{L}_{S_{2D}}$ use standard L1 loss.

Following the MonoDLE paradigm [14], the 3D object loss trains the network to predict key 3D attributes. It includes the 3D center offset loss $\mathcal{L}_{O_{3D}}$ and 3D size loss $\mathcal{L}_{S_{3D}}$ with L1 loss, the orientation loss \mathcal{L}_{θ} using multi-bin loss [72], and the depth loss \mathcal{L}_D supervised by Laplacian aleatoric uncertainty loss [52]:

$$\mathcal{L}_{3D} = \mathcal{L}_{O_{3D}} + \mathcal{L}_{S_{3D}} + \mathcal{L}_{\theta} + \mathcal{L}_D. \quad (19)$$

IV. EXPERIMENTS

A. Setup

1) *Dataset*: To evaluate the performance of our proposed method, we conducted experiments on the KITTI 3D object detection benchmark [33] and Waymo Open dataset [34]. The KITTI dataset consists of 7,481 training images and 7,518 testing images. It includes three primary object classes: Car, Pedestrian, and Cyclist, with varying levels of difficulty (*Easy*, *Moderate*, and *Hard*) based on factors such as object size, occlusion, and truncation. Following the previous studies [73], the training images are further split into a training set of 3,712 images and a validation set of 3,769 images.

The Waymo Open Dataset [34] is a pivotal resource for autonomous driving scene understanding, featuring 798 training and 202 validation sequences, yielding approximately 160,000 and 40,000 samples, respectively. For our experiments, we adopt the approach from [73], generating 52,386 training images and 39,848 validation images by sampling every third frame from the training sequences. This dataset captures diverse real-world driving scenarios and categorizes objects into LEVEL_1 and LEVEL_2 based on LiDAR point density.

2) *Evaluation metrics*: In KITTI, model’s performance is typically measured using average precision in 3D space and birds-eye view (AP_{3D} and AP_{BEV}) at 40 recall positions. The AP is calculated based on Intersection over Union between the predicted 3D bounding boxes and the ground truth, with specific IoU thresholds for each object class – 0.7 for cars and 0.5 for pedestrians and cyclists. Following the official protocol [33], we use AP_{3D} and AP_{BEV} on *Moderate* category as main metrics. In Waymo, evaluations use two IoU thresholds (0.5 and 0.7) across four distance ranges: Overall, 0 - 30m, 30 - 50m, and 50m - ∞ .

3) *Data augmentation*: To enhance the generalization ability of our model, we incorporated several data augmentation techniques commonly used in object detection. During training, we applied random horizontal flipping and random cropping with a probability of 0.5, random scaling with a probability of 0.4,

TABLE I
COMPARISONS FOR THE CAR CATEGORY ON THE KITTI TEST SET AT IoU = 0.7. THE BEST AND SECOND BEST RESULTS ARE BOLDED AND UNDERLINED, RESPECTIVELY. THE IMPROVEMENTS ARE SHOWN IN PURPLE FONTS.

Methods	Reference	Extra Data	Test, $AP_{3D R40}(\%)$			Test, $AP_{BEV R40}(\%)$		
			Easy	Mod.	Hard	Easy	Mod.	Hard
D4LCN [40]	CVPR 2020	Depth	16.65	11.72	9.51	22.51	16.02	12.55
Kinematic3D [11]	ECCV 2020	Multi-frames	19.07	12.72	9.17	26.99	17.52	13.10
MonoRUn [3]	CVPR 2021	LiDAR	19.65	12.30	10.58	27.94	17.34	15.24
CaDDN [4]	CVPR 2021	LiDAR	19.17	13.41	11.46	27.94	18.91	17.19
AutoShape [9]	ICCV 2021	CAD	22.47	14.17	11.36	30.66	20.08	15.59
MonoDTR [5]	CVPR 2022	LiDAR	21.99	15.39	12.73	28.59	20.38	17.14
DCD [10]	ECCV 2022	CAD	23.81	15.90	13.21	32.55	21.50	18.25
SMOKE [13]	CVPRW 2020	None	14.03	9.76	7.84	20.83	14.49	12.75
MonoDLE [14]	CVPR 2021	None	17.23	12.26	10.29	24.79	18.89	16.00
GUPNet [21]	ICCV 2021	None	20.11	14.20	11.77	-	-	-
MonoGround [25]	CVPR 2022	None	21.37	14.36	12.62	30.07	20.47	17.74
DEVIANT [22]	ECCV 2022	None	21.88	14.46	11.89	29.65	20.44	17.43
MonoCon [16]	AAAI 2022	None	22.50	16.46	13.95	31.12	22.10	19.00
MonoDDE [24]	CVPR 2022	None	24.93	17.14	15.10	33.58	23.46	20.37
PDR [59]	TCSVT 2023	None	23.69	16.14	13.78	31.76	21.74	18.79
DVDET [76]	RAL 2023	None	23.19	15.44	13.07	32.05	22.15	19.32
MonoDETR [65]	ICCV 2023	None	25.00	16.47	13.58	33.60	22.11	18.60
MonoCD [27]	CVPR 2024	None	25.53	16.59	14.53	33.41	22.81	19.57
FD3D [75]	AAAI 2024	None	25.38	17.12	14.50	<u>34.20</u>	<u>23.72</u>	<u>20.76</u>
MonoASRH(Ours)	-	None	26.18	19.17	16.92	34.84	25.89	22.48
<i>Improvement</i>	-	<i>v.s. second-best</i>	+0.65	+2.03	+1.82	+0.64	+2.17	+1.72

and random shifting with a probability of 0.1. Additionally, we utilized the MixUp3D technique from MonoLSS [17] as an extra data augmentation strategy to further improve the model’s robustness against occlusions.

4) *Implementation details:* Our proposed MonoASRH was trained on two RTX 3090 GPUs with batch size of 16. For the EH-FAM, we set the channel dimension d_v of V_i to 128 in the multi-head self-attention. Following [21], the RoI-Align size $d \times d$ is set to 7×7 . For KITTI, we trained the model for 450 epochs using the Adam optimizer [74], with a weight decay of $1e-5$. The initial learning rate was set to $1e-3$ and decayed by a factor of 10 at the 250th and 370th epochs. For Waymo Open dataset, we trained the model for only 80 epochs with a batch size of 32, while keeping all other settings consistent with those used for KITTI. During testing, the maximum number of detectable objects per image, K , was set to 50.

B. Main Results

We compared our proposed MonoASRH with state-of-the-art monocular 3D object detection methods on the KITTI test set for the car category. As shown in Table I, our method outperformed the CAD model-based DCD [10], even without additional data. Compared to other methods that do not use extra data, MonoASRH achieved improvements in $AP_{3D|R40}$ across all three difficulty levels by 0.65%, 2.03%, and 1.82%. Additionally, it surpassed the top-performing FD3D [75] in $AP_{BEV|R40}$ by 0.64%, 2.17%, and 1.72%. Experimental results validate the effectiveness of our method in detecting objects in the Car category.

The results for the Pedestrian and Cyclist categories in the KITTI test set are presented in Table II. For Pedestrians, MonoASRH achieved the best performance across all difficulty levels, outperforming the LiDAR-based MonoDTR method [5]. In the Cyclist category, MonoASRH ranked third at the *Easy* level but still showed competitive performance,

TABLE II
COMPARISONS FOR THE PEDESTRIAN AND CYCLIST CATEGORY ON THE KITTI TEST SET AT IoU = 0.5. THE BEST AND SECOND BEST RESULTS ARE BOLDED AND UNDERLINED, RESPECTIVELY.

Methods	Extra Data	Test, $AP_{3D R40}(\%)$					
		Pedestrian			Cyclist		
		Easy	Mod.	Hard	Easy	Mod.	Hard
CaDDN [4]	LiDAR	12.87	8.14	6.76	7.00	3.41	3.30
MonoDTR [5]	LiDAR	<u>15.33</u>	<u>10.18</u>	<u>8.61</u>	5.05	3.27	3.19
DCD [10]	CAD	10.37	6.73	6.28	4.27	2.74	2.41
DEVIANT [22]	None	13.43	8.65	7.69	5.05	3.13	2.59
MonoCon [16]	None	13.10	8.41	6.94	2.80	1.92	1.55
MonoDDE [24]	None	11.13	7.32	6.67	5.94	3.78	<u>3.33</u>
PDR [59]	None	11.61	7.72	6.40	2.72	1.57	1.50
MonoDETR [65]	None	12.54	7.89	6.65	7.33	4.18	2.92
MonoASRH(Ours)	None	16.90	11.24	9.64	6.49	3.94	3.51

TABLE III
PERFORMANCE OF THE CAR CATEGORY ON THE KITTI VALIDATION SET AT IoU = 0.7. THE BEST AND SECOND BEST RESULTS ARE BOLDED AND UNDERLINED, RESPECTIVELY.

Methods	Val, $AP_{3D R40}(\%)$			Val, $AP_{BEV R40}(\%)$		
	Easy	Mod.	Hard	Easy	Mod.	Hard
GUPNet [21]	22.76	16.46	13.72	31.07	22.94	19.75
DEVIANT [22]	24.63	16.54	14.52	32.60	23.04	19.99
MonoDDE [24]	26.66	19.75	16.72	35.51	26.48	23.07
PDR [59]	27.65	19.44	16.24	35.59	25.72	21.35
MonoDETR [65]	28.84	<u>20.61</u>	16.38	-	-	-
MonoCD [27]	26.45	19.37	16.38	34.60	24.96	21.51
MonoLSS [17]	25.91	18.29	15.94	34.70	25.36	21.84
FD3D [75]	28.22	20.23	<u>17.04</u>	<u>36.98</u>	<u>26.77</u>	<u>23.16</u>
MonoASRH(Ours)	<u>28.35</u>	20.75	17.56	37.53	27.26	24.16

with a slight drop at the *Moderate* level compared to the Transformer-based MonoDETR [65]. However, it achieved the best performance at the *Hard* level with a 3.51% $AP_{3D|R40}$. These results highlight the challenges of detecting smaller, non-rigid objects like Pedestrians and Cyclists. Nonetheless, MonoASRH’s scale-aware dynamic receptive field adjustment capability enabled strong performance in these categories, validating the model’s generalization and scalability. Additionally,



Fig. 6. Qualitative results produced by the proposed MonoASRH on the KITTI test set. The detected 3D bounding boxes for Car, Pedestrian and Cyclist are shown in purple, orange and green, respectively.

TABLE IV
COMPARISONS FOR THE VEHICLE CATEGORY ON THE WAYMO OPEN VALIDATION SET. WE USE AP_{3D} (LEVEL_1 AND LEVEL_2, IOU > 0.5 AND IOU > 0.7) ACCORDING TO THREE OBJECT DISTANCE INTERVALS.

Methods	Reference	LEVEL_1(IoU > 0.5)				LEVEL_2(IoU > 0.5)				LEVEL_1(IoU > 0.7)				LEVEL_2(IoU > 0.7)			
		Overall	0-30m	30-50m	50m-Inf	Overall	0-30m	30-50m	50m-Inf	Overall	0-30m	30-50m	50m-Inf	Overall	0-30m	30-50m	50m-Inf
With extra data:																	
PatchNet [42]	ECCV 2020	2.92	10.03	1.09	0.23	2.42	10.01	1.07	0.22	0.39	1.67	0.13	0.03	0.38	1.67	0.13	0.03
PCT [77]	NIPS 2021	4.20	14.70	1.78	0.39	4.03	14.67	1.74	0.36	0.89	3.18	0.27	0.07	0.66	3.18	0.27	0.07
Without extra data:																	
GUPNet [21]	ICCV 2021	10.02	24.78	4.84	0.22	9.39	24.69	4.67	0.19	2.28	6.15	0.81	0.03	2.14	6.13	0.78	0.02
MonoJSG [53]	CVPR 2022	5.65	20.86	3.91	<u>0.97</u>	5.34	20.79	3.79	<u>0.85</u>	0.97	4.65	0.55	<u>0.10</u>	0.91	4.64	0.55	<u>0.09</u>
DEVIANT [22]	ECCV 2022	10.98	26.85	<u>5.13</u>	0.18	10.29	26.75	<u>4.95</u>	0.16	2.69	6.95	<u>0.99</u>	0.02	2.52	6.93	<u>0.95</u>	0.02
MonoRCNN++ [78]	WACV 2023	<u>11.37</u>	<u>27.95</u>	4.07	0.42	<u>10.79</u>	<u>27.88</u>	3.98	0.39	4.28	9.84	0.91	0.09	4.05	9.81	0.89	0.08
MonoASRH(Ours)	-	12.35	29.25	6.16	1.10	11.58	29.14	5.95	0.96	3.36	9.49	1.01	0.13	3.15	9.46	0.97	0.11

the decoupled convolutional layers in EH-FAM are better equipped to capture the features of these categories with large aspect ratios.

As shown in Table III, MonoASRH was also evaluated on the KITTI validation set. For the Car category at the 0.7 IoU threshold and *Moderate* difficulty, MonoASRH achieved state-of-the-art performance with $AP_{3D|R40}$ and $AP_{BEV|R40}$ scores of 20.75% and 27.26%, respectively. Some qualitative results on the KITTI test set are shown in Fig. 6. Benefiting from the globally-aware self-attention mechanism in EH-FAM, the model effectively captures long-range dependencies for smaller objects such as distant cars.

Table IV compares the AP_{3D} metrics for the ‘‘Vehicle’’ category across various methods on the Waymo Open Val Set. In both the 30-50m and 50m-Inf ranges, our model achieved state-of-the-art performance. Compared to MonoRCNN++ [78], MonoASRH improved the AP_{3D} by 2.09% and 0.10% at IoU thresholds of 0.5 and 0.7, respectively, within the 30-50m range under the LEVEL 1 setting. Additionally, under the LEVEL 2 setting, the AP_{3D} metrics improved by 1.97% and 0.08% at different IoU thresholds within the 30-50m range. These results further validate the effectiveness of MonoASRH in detecting distant and small objects.

C. Ablation Studies

In this section, we evaluate the impact of each component of the proposed framework on the network’s performance. Ablation studies were conducted on the KITTI validation set

TABLE V
ABLATION STUDY ON DIFFERENT COMPONENTS OF OUR OVERALL FRAMEWORK ON KITTI VAL SET FOR CAR CATEGORY. ‘A’, ‘E’ AND ‘ \mathcal{L}_H ’ DENOTE ADAPTIVE SCALE-AWARE 3D REGRESSION HEAD, EFFICIENT HYBRID FEATURE AGGREGATION MODULE, AND SELECTIVE CONFIDENCE-GUIDED HEATMAP LOSS, RESPECTIVELY.

A	E	\mathcal{L}_H	Val, $AP_{3D R40}$ (%)		
			Easy	Mod.	Hard
-	-	-	25.30	18.20	15.80
✓	-	-	26.12	20.32	17.34
-	✓	-	26.67	19.39	16.11
-	-	✓	25.87	18.23	15.76
✓	✓	-	27.98	20.73	17.45
✓	✓	✓	28.35	20.75	17.56

using the Car category, with $AP_{3D|R40}$ and $AP_{BEV|R40}$ as metrics. Our baseline model is based on the GUPNet [21] and incorporates the Learnable Sample Selection from MonoLSS [17] for initial training. We compare the effects of different components, including the Adaptive Scale-Aware 3D Regression Head, Efficient Hybrid Feature Aggregation Module, and Selective Confidence-Guided Heatmap Loss. The results in Table V demonstrate the contributions of each module to the overall performance of our method.

1) *Adaptive Scale-Aware 3D Regression Head*: In Table VI, we further explore the contribution of each component within the Adaptive Scale-Aware 3D Regression Head to model’s performance. Specifically, we evaluated ASRH under three settings: ‘‘w/o Scale-Aware Offset’’, where receptive field offsets are derived solely from semantic features without object

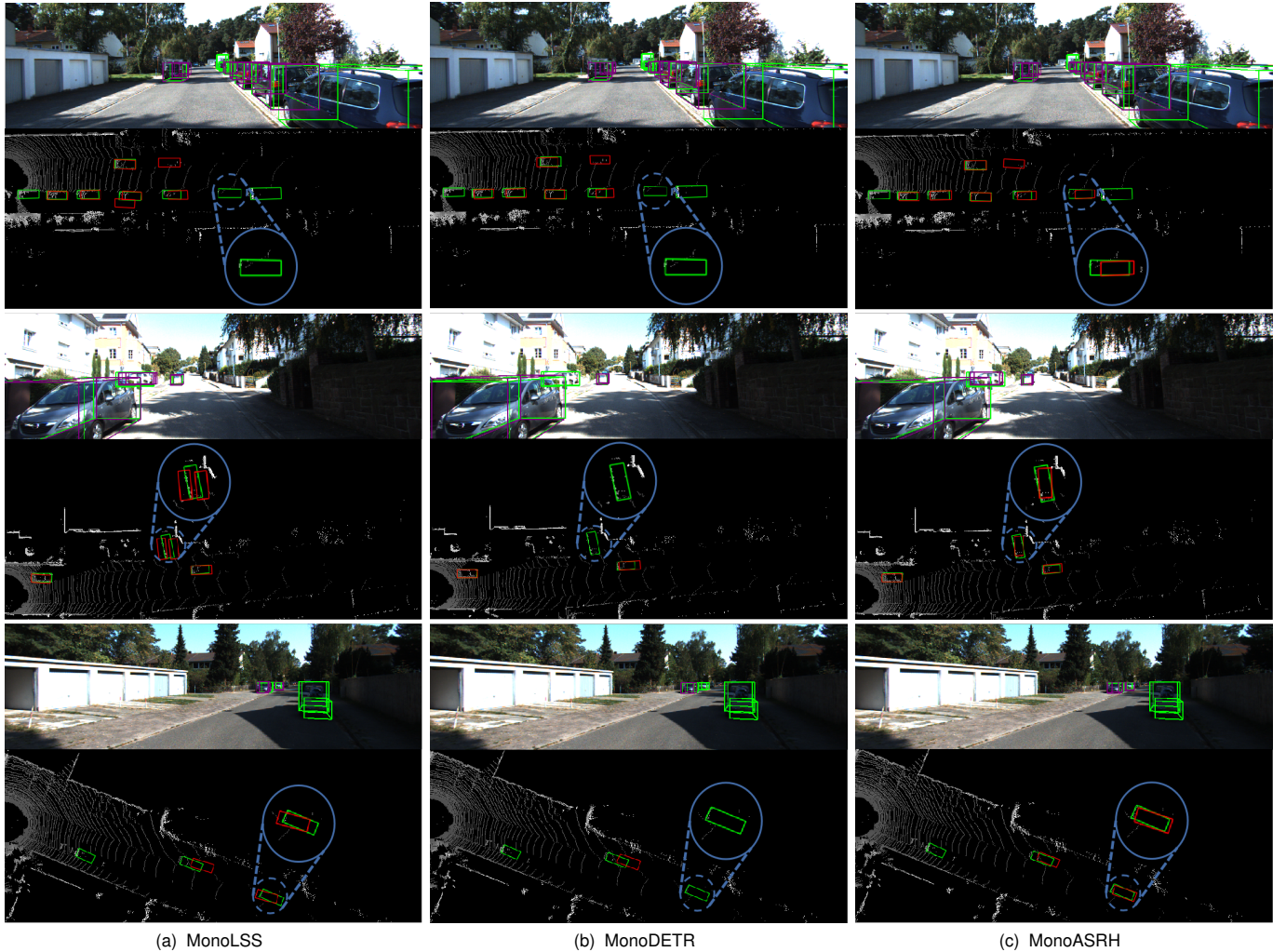


Fig. 7. Qualitative comparison results of 3D object detection on the KITTI val set: (a) MonoLSS [17], (b) MonoDETR [65], and (c) Ours. In each group of images, the first row shows the camera view, and the second row shows the BEV view. In the camera view, predicted and ground truth 3D bounding boxes are shown in purple and green, respectively. In the BEV view, their projections are represented in red and green.

TABLE VI
ABLATION STUDY OF ASRH ON KITTI VAL SET FOR CAR CATEGORY.

Architecture	Val, $AP_{3D R40}(\%)$		
	Easy	Mod.	Hard
Baseline + ASRH	26.12	20.32	17.34
w/o Scale-Aware Offset	25.72	18.91	16.35
w/o Adaptive Attention Mask	25.63	19.86	17.00
w/o Attentive Normalization	25.97	20.15	17.16

TABLE VII
COMPARISON EXPERIMENT BETWEEN ASRH AND DEFORMABLE CONVOLUTION ON KITTI VAL SET FOR CAR CATEGORY. ‘Deform.’ DENOTES DEFORMABLE CONVOLUTION.

Methods	Val, $AP_{3D R40}(\%)$			Val, $AP_{BEV R40}(\%)$		
	Easy	Mod.	Hard	Easy	Mod.	Hard
Baseline	25.30	18.20	15.80	34.41	25.50	21.86
+ Deform.	25.71	18.85	16.88	34.55	25.80	22.27
+ ASRH	26.12	20.32	17.34	35.26	27.36	23.87

scale information; “w/o Adaptive Attention Mask”, where the attention mask is randomly initialized; “w/o Attentive Normalization”, where the AN layer [70] is not applied to normalize feature maps F_{de} . The experimental results show that incorporating scale information is crucial in ASRH, enabling the model to perform dynamic scale-aware adjustments of the receptive field. This significantly improves detection, particularly for small and occluded objects at *Moderate* and *Hard* difficulty levels.

Additionally, we compared ASRH with the standard deformable convolution [30]. We inserted deformable convolution into the first layer of each 3D regression head in

the baseline model and conducted comparison experiments with ASRH. As shown in Table VII, ASRH consistently outperformed standard deformable convolutions in monocular 3D detection tasks.

2) *Efficient Hybrid Feature Aggregation Module*: To further validate the generalization capability of EH-FAM as a plug-and-play module for monocular 3D object detection, we conducted ablation studies on different baseline models, as shown in Table VIII. In these experiments, we replaced the original feature aggregation modules (e.g., DLAUp [32]) in each baseline model with EH-FAM and compared the $AP_{3D|R40}$ scores, parameters, and computational costs before

TABLE VIII
ABLATION STUDY OF EH-FAM WITH DIFFERENT BASELINES ON KITTI
VAL SET FOR CAR CATEGORY. ‘⊕’ INDICATES THAT THE FEATURE
AGGREGATION MODULE OF THE ORIGINAL BASELINE MODEL IS
REPLACED WITH EH-FAM.

Methods	Val. $AP_{3D R40}$ (%)			Params(M)↓	FLOPs(G)↓
	Easy	Mod.	Hard		
MonoDLE [14]	17.45	13.66	11.68	19.86	158.18
MonoDLE ⊕ EH-FAM	19.89	14.41	12.35	18.12	149.14
Improvement	+2.44	+0.75	+0.67	-8.76%	-5.71%
GUPNet [21]	22.76	16.46	13.72	19.90	124.57
GUPNet ⊕ EH-FAM	22.90	16.51	13.92	18.16	115.53
Improvement	+0.14	+0.05	+0.20	-8.74%	-7.25%
MonoLSS [17]	25.91	18.29	15.94	20.51	126.13
MonoLSS ⊕ EH-FAM	26.62	19.30	16.09	18.77	117.09
Improvement	+0.71	+1.01	+0.15	-8.48%	-7.17%

and after the replacement (with computations evaluated using a batch size of 1). The results in Table VIII show that EH-FAM led to performance improvements and parameter reduction across all three baselines. Specifically, the $AP_{3D|R40}$ scores for MonoDLE [14], GUPNet [21], and MonoLSS [17] on the *Moderate* level increased by 0.75%, 0.05%, and 0.91%, respectively, while their parameter counts decreased by 8.76%, 8.74%, and 8.48%. Additionally, the computational cost was reduced by 5.71%, 7.25%, and 7.17%, respectively. These results confirm that EH-FAM can be widely applied to various baselines, significantly enhancing both performance and computational efficiency.

3) *Selective Confidence-Guided Heatmap Loss*: The Selective Confidence-Guided Heatmap Loss guides the network to focus more on high-confidence samples. As shown in Table V, when used alone, this loss achieves the largest improvement in the baseline model’s $AP_{3D|R40}$ for the Car category at the *Easy* level, reaching 25.87%. When using the other two modules, adding the loss further improves the $AP_{3D|R40}$ by 0.37%. This demonstrates that the loss function is particularly beneficial for detecting *Easy* samples in the KITTI dataset. The likely reason is that the loss encourages the model to rely more on high-confidence detections, and *Easy* samples are generally easier to detect, leading to higher confidence scores.

D. Visualization

In Fig. 7, we compare the proposed MonoASRH with the Transformer-based MonoDETR [65] and center-based MonoLSS [17]. Each group of images shows the camera view and BEV view. Compared to the other methods, MonoASRH produces higher-quality 3D bounding boxes across various scenes. Notably, it excels at detecting and localizing small distant objects, such as the white vehicle on the right in the third group of images, demonstrating the benefit of incorporating scale information. MonoASRH also provides more accurate results for fully visible objects. Additionally, it more effectively detects partially occluded objects, as shown on the left in the second group of images.

V. CONCLUSION

We propose MonoASRH, which introduces Efficient Hybrid Feature Aggregation Module (EH-FAM) and Scale-Aware 3D

Regression Head (ASRH) for monocular 3D detection. Our plug-and-play EH-FAM employs a hybrid architecture to efficiently aggregate features across different scales, endowing the model with richer scale-aware semantic information. ASRH dynamically adjusts the network’s receptive field according to the scale of objects, thereby enhancing 3D detection accuracy. Experimental results on the KITTI and Waymo benchmark demonstrate that MonoASRH achieves state-of-the-art performance. However, MonoASRH may underperform when detecting truncated objects, as these objects often lead to inaccuracies in the acquisition of scale features by ASRH. Future research will focus on overcoming this challenge.

REFERENCES

- [1] E. Arnold, O. Y. Al-Jarrah, M. Dianati, S. Fallah, D. Oxtoby, and A. Mouzakitis, “A survey on 3d object detection methods for autonomous driving applications,” *IEEE Transactions on Intelligent Transportation Systems*, vol. 20, no. 10, pp. 3782–3795, 2019.
- [2] S. Grigorescu, B. Trane, T. Cocias, and G. Macesanu, “A survey of deep learning techniques for autonomous driving,” *Journal of field robotics*, vol. 37, no. 3, pp. 362–386, 2020.
- [3] H. Chen, Y. Huang, W. Tian, Z. Gao, and L. Xiong, “Monorun: Monocular 3d object detection by reconstruction and uncertainty propagation,” in *Proceedings of the IEEE/CVF Conference on Computer Vision and Pattern Recognition*, 2021, pp. 10 379–10 388.
- [4] C. Reading, A. Harakeh, J. Chae, and S. L. Waslander, “Categorical depth distribution network for monocular 3d object detection,” in *Proceedings of the IEEE/CVF Conference on Computer Vision and Pattern Recognition*, 2021, pp. 8555–8564.
- [5] K.-C. Huang, T.-H. Wu, H.-T. Su, and W. H. Hsu, “Monodtr: Monocular 3d object detection with depth-aware transformer,” in *Proceedings of the IEEE/CVF conference on computer vision and pattern recognition*, 2022, pp. 4012–4021.
- [6] Z. Chong, X. Ma, H. Zhang, Y. Yue, H. Li, Z. Wang, and W. Ouyang, “Monodistill: Learning spatial features for monocular 3d object detection,” *arXiv preprint arXiv:2201.10830*, 2022.
- [7] C. Li, J. Ku, and S. L. Waslander, “Confidence guided stereo 3d object detection with split depth estimation,” in *2020 IEEE/RSJ international conference on intelligent robots and systems (IROS)*. IEEE, 2020, pp. 5776–5783.
- [8] Z. Zhou, L. Du, X. Ye, Z. Zou, X. Tan, L. Zhang, X. Xue, and J. Feng, “Sgm3d: Stereo guided monocular 3d object detection,” *IEEE Robotics and Automation Letters*, vol. 7, no. 4, pp. 10 478–10 485, 2022.
- [9] Z. Liu, D. Zhou, F. Lu, J. Fang, and L. Zhang, “Autoshape: Real-time shape-aware monocular 3d object detection,” in *Proceedings of the IEEE/CVF International Conference on Computer Vision*, 2021, pp. 15 641–15 650.
- [10] Y. Li, Y. Chen, J. He, and Z. Zhang, “Densely constrained depth estimator for monocular 3d object detection,” in *European Conference on Computer Vision*. Springer, 2022, pp. 718–734.
- [11] G. Brazil, G. Pons-Moll, X. Liu, and B. Schiele, “Kinematic 3d object detection in monocular video,” in *Computer Vision—ECCV 2020: 16th European Conference, Glasgow, UK, August 23–28, 2020, Proceedings, Part XXIII 16*. Springer, 2020, pp. 135–152.
- [12] X. Zhou, D. Wang, and P. Krähenbühl, “Objects as points,” *arXiv preprint arXiv:1904.07850*, 2019.
- [13] Z. Liu, Z. Wu, and R. Tóth, “Smoke: Single-stage monocular 3d object detection via keypoint estimation,” in *Proceedings of the IEEE/CVF conference on computer vision and pattern recognition workshops*, 2020, pp. 996–997.
- [14] X. Ma, Y. Zhang, D. Xu, D. Zhou, S. Yi, H. Li, and W. Ouyang, “Delving into localization errors for monocular 3d object detection,” in *Proceedings of the IEEE/CVF Conference on Computer Vision and Pattern Recognition*, 2021, pp. 4721–4730.
- [15] S. Luo, H. Dai, L. Shao, and Y. Ding, “M3dssd: Monocular 3d single stage object detector,” in *Proceedings of the IEEE/CVF conference on computer vision and pattern recognition*, 2021, pp. 6145–6154.
- [16] X. Liu, N. Xue, and T. Wu, “Learning auxiliary monocular contexts helps monocular 3d object detection,” in *Proceedings of the AAAI Conference on Artificial Intelligence*, vol. 36, no. 2, 2022, pp. 1810–1818.

- [17] Z. Li, J. Jia, and Y. Shi, “Monolss: Learnable sample selection for monocular 3d detection,” in *2024 International Conference on 3D Vision (3DV)*. IEEE, 2024, pp. 1125–1135.
- [18] K. Duan, S. Bai, L. Xie, H. Qi, Q. Huang, and Q. Tian, “Centernet: Keypoint triplets for object detection,” in *Proceedings of the IEEE/CVF international conference on computer vision*, 2019, pp. 6569–6578.
- [19] P. Li, H. Zhao, P. Liu, and F. Cao, “Rtm3d: Real-time monocular 3d detection from object keypoints for autonomous driving,” in *European Conference on Computer Vision*. Springer, 2020, pp. 644–660.
- [20] Y. Zhang, J. Lu, and J. Zhou, “Objects are different: Flexible monocular 3d object detection,” in *Proceedings of the IEEE/CVF Conference on Computer Vision and Pattern Recognition*, 2021, pp. 3289–3298.
- [21] Y. Lu, X. Ma, L. Yang, T. Zhang, Y. Liu, Q. Chu, J. Yan, and W. Ouyang, “Geometry uncertainty projection network for monocular 3d object detection,” in *Proceedings of the IEEE/CVF International Conference on Computer Vision*, 2021, pp. 3111–3121.
- [22] A. Kumar, G. Brazil, E. Corona, A. Parchami, and X. Liu, “Deviant: Depth equivariant network for monocular 3d object detection,” in *European Conference on Computer Vision*. Springer, 2022, pp. 664–683.
- [23] Y. Kim, S. Kim, S. Sim, J. W. Choi, and D. Kum, “Boosting monocular 3d object detection with object-centric auxiliary depth supervision,” *IEEE Transactions on Intelligent Transportation Systems*, vol. 24, no. 2, pp. 1801–1813, 2022.
- [24] Z. Li, Z. Qu, Y. Zhou, J. Liu, H. Wang, and L. Jiang, “Diversity matters: Fully exploiting depth clues for reliable monocular 3d object detection,” in *Proceedings of the IEEE/CVF Conference on Computer Vision and Pattern Recognition*, 2022, pp. 2791–2800.
- [25] Z. Qin and X. Li, “Monoground: Detecting monocular 3d objects from the ground,” in *Proceedings of the IEEE/CVF Conference on Computer Vision and Pattern Recognition*, 2022, pp. 3793–3802.
- [26] M. Zhu, L. Ge, P. Wang, and H. Peng, “Monoedge: Monocular 3d object detection using local perspectives,” in *Proceedings of the IEEE/CVF Winter Conference on Applications of Computer Vision*, 2023, pp. 643–652.
- [27] L. Yan, P. Yan, S. Xiong, X. Xiang, and Y. Tan, “Monocd: Monocular 3d object detection with complementary depths,” in *Proceedings of the IEEE/CVF Conference on Computer Vision and Pattern Recognition*, 2024, pp. 10248–10257.
- [28] W. Chen, J. Zhao, W.-L. Zhao, and S.-Y. Wu, “Shape-aware monocular 3d object detection,” *IEEE Transactions on Intelligent Transportation Systems*, vol. 24, no. 6, pp. 6416–6424, 2023.
- [29] J.-H. Chen, J.-L. Shieh, M. A. Haq, and S.-J. Ruan, “Monocular 3d object detection utilizing auxiliary learning with deformable convolution,” *IEEE Transactions on Intelligent Transportation Systems*, 2023.
- [30] X. Zhu, H. Hu, S. Lin, and J. Dai, “Deformable convnets v2: More deformable, better results,” in *Proceedings of the IEEE/CVF conference on computer vision and pattern recognition*, 2019, pp. 9308–9316.
- [31] Y. Zhao, W. Lv, S. Xu, J. Wei, G. Wang, Q. Dang, Y. Liu, and J. Chen, “Detsr beat yolos on real-time object detection,” in *Proceedings of the IEEE/CVF Conference on Computer Vision and Pattern Recognition*, 2024, pp. 16965–16974.
- [32] F. Yu, D. Wang, E. Shelhamer, and T. Darrell, “Deep layer aggregation,” in *Proceedings of the IEEE conference on computer vision and pattern recognition*, 2018, pp. 2403–2412.
- [33] A. Geiger, P. Lenz, and R. Urtasun, “Are we ready for autonomous driving? the kitti vision benchmark suite,” in *2012 IEEE conference on computer vision and pattern recognition*. IEEE, 2012, pp. 3354–3361.
- [34] P. Sun, H. Kretschmar, X. Dotiwalla, A. Chouard, V. Patnaik, P. Tsui, J. Guo, Y. Zhou, Y. Chai, B. Caine *et al.*, “Scalability in perception for autonomous driving: Waymo open dataset,” in *Proceedings of the IEEE/CVF conference on computer vision and pattern recognition*, 2020, pp. 2446–2454.
- [35] X. Wang, W. Yin, T. Kong, Y. Jiang, L. Li, and C. Shen, “Task-aware monocular depth estimation for 3d object detection,” in *Proceedings of the AAAI Conference on Artificial Intelligence*, vol. 34, no. 07, 2020, pp. 12257–12264.
- [36] H. Fu, M. Gong, C. Wang, K. Batmanghelich, and D. Tao, “Deep ordinal regression network for monocular depth estimation,” in *Proceedings of the IEEE conference on computer vision and pattern recognition*, 2018, pp. 2002–2011.
- [37] J. H. Lee, M.-K. Han, D. W. Ko, and I. H. Suh, “From big to small: Multi-scale local planar guidance for monocular depth estimation,” *arXiv preprint arXiv:1907.10326*, 2019.
- [38] C. Godard, O. Mac Aodha, M. Firman, and G. J. Brostow, “Digging into self-supervised monocular depth estimation,” in *Proceedings of the IEEE/CVF international conference on computer vision*, 2019, pp. 3828–3838.
- [39] V. Guizilini, R. Ambrus, S. Pillai, A. Raventos, and A. Gaidon, “3d packing for self-supervised monocular depth estimation,” in *Proceedings of the IEEE/CVF conference on computer vision and pattern recognition*, 2020, pp. 2485–2494.
- [40] M. Ding, Y. Huo, H. Yi, Z. Wang, J. Shi, Z. Lu, and P. Luo, “Learning depth-guided convolutions for monocular 3d object detection,” in *Proceedings of the IEEE/CVF Conference on computer vision and pattern recognition workshops*, 2020, pp. 1000–1001.
- [41] L. Wang, L. Du, X. Ye, Y. Fu, G. Guo, X. Xue, J. Feng, and L. Zhang, “Depth-conditioned dynamic message propagation for monocular 3d object detection,” in *Proceedings of the IEEE/CVF Conference on Computer Vision and Pattern Recognition*, 2021, pp. 454–463.
- [42] X. Ma, S. Liu, Z. Xia, H. Zhang, X. Zeng, and W. Ouyang, “Rethinking pseudo-lidar representation,” in *Computer Vision—ECCV 2020: 16th European Conference, Glasgow, UK, August 23–28, 2020, Proceedings, Part XIII 16*. Springer, 2020, pp. 311–327.
- [43] X. Weng and K. Kitani, “Monocular 3d object detection with pseudo-lidar point cloud,” in *Proceedings of the IEEE/CVF International Conference on Computer Vision Workshops*, 2019, pp. 0–0.
- [44] X. Ma, Z. Wang, H. Li, P. Zhang, W. Ouyang, and X. Fan, “Accurate monocular 3d object detection via color-embedded 3d reconstruction for autonomous driving,” in *Proceedings of the IEEE/CVF international conference on computer vision*, 2019, pp. 6851–6860.
- [45] Y. Wang, W.-L. Chao, D. Garg, B. Hariharan, M. Campbell, and K. Q. Weinberger, “Pseudo-lidar from visual depth estimation: Bridging the gap in 3d object detection for autonomous driving,” in *Proceedings of the IEEE/CVF conference on computer vision and pattern recognition*, 2019, pp. 8445–8453.
- [46] F. Manhardt, W. Kehl, and A. Gaidon, “Roi-10d: Monocular lifting of 2d detection to 6d pose and metric shape,” in *Proceedings of the IEEE/CVF Conference on Computer Vision and Pattern Recognition*, 2019, pp. 2069–2078.
- [47] S. Pillai, R. Ambrus, and A. Gaidon, “Superdepth: Self-supervised, super-resolved monocular depth estimation,” in *2019 International Conference on Robotics and Automation (ICRA)*. IEEE, 2019, pp. 9250–9256.
- [48] B. Xu and Z. Chen, “Multi-level fusion based 3d object detection from monocular images,” in *Proceedings of the IEEE conference on computer vision and pattern recognition*, 2018, pp. 2345–2353.
- [49] Y. You, Y. Wang, W.-L. Chao, D. Garg, G. Pleiss, B. Hariharan, M. Campbell, and K. Q. Weinberger, “Pseudo-lidar++: Accurate depth for 3d object detection in autonomous driving,” *arXiv preprint arXiv:1906.06310*, 2019.
- [50] A. Simonelli, S. R. Buló, L. Porzi, M. López-Antequera, and P. Kotschieder, “Disentangling monocular 3d object detection,” in *Proceedings of the IEEE/CVF International Conference on Computer Vision*, 2019, pp. 1991–1999.
- [51] A. Simonelli, S. R. Buló, L. Porzi, P. Kotschieder, and E. Ricci, “Are we missing confidence in pseudo-lidar methods for monocular 3d object detection?” in *Proceedings of the IEEE/CVF International Conference on Computer Vision*, 2021, pp. 3225–3233.
- [52] Y. Chen, L. Tai, K. Sun, and M. Li, “Monopair: Monocular 3d object detection using pairwise spatial relationships,” in *Proceedings of the IEEE/CVF Conference on Computer Vision and Pattern Recognition*, 2020, pp. 12093–12102.
- [53] Q. Lian, P. Li, and X. Chen, “Monojsr: Joint semantic and geometric cost volume for monocular 3d object detection,” in *Proceedings of the IEEE/CVF Conference on Computer Vision and Pattern Recognition*, 2022, pp. 1070–1079.
- [54] T. Yin, X. Zhou, and P. Krahenbuhl, “Center-based 3d object detection and tracking,” in *Proceedings of the IEEE/CVF conference on computer vision and pattern recognition*, 2021, pp. 11784–11793.
- [55] Y. Zhou, Y. He, H. Zhu, C. Wang, H. Li, and Q. Jiang, “Monoef: Extrinsic parameter free monocular 3d object detection,” *IEEE Transactions on Pattern Analysis and Machine Intelligence*, vol. 44, no. 12, pp. 10114–10128, 2021.
- [56] A. Kendall, Y. Gal, and R. Cipolla, “Multi-task learning using uncertainty to weigh losses for scene geometry and semantics,” in *Proceedings of the IEEE conference on computer vision and pattern recognition*, 2018, pp. 7482–7491.
- [57] J. Gu, B. Wu, L. Fan, J. Huang, S. Cao, Z. Xiang, and X.-S. Hua, “Homography loss for monocular 3d object detection,” in *Proceedings of the IEEE/CVF Conference on Computer Vision and Pattern Recognition*, 2022, pp. 1080–1089.

- [58] H. Yao, J. Chen, Z. Wang, X. Wang, P. Han, X. Chai, and Y. Qiu, "Occlusion-aware plane-constraints for monocular 3d object detection," *IEEE Transactions on Intelligent Transportation Systems*, 2023.
- [59] H. Sheng, S. Cai, N. Zhao, B. Deng, M.-J. Zhao, and G. H. Lee, "Pdr: Progressive depth regularization for monocular 3d object detection," *IEEE Transactions on Circuits and Systems for Video Technology*, vol. 33, no. 12, pp. 7591–7603, 2023.
- [60] E. Jang, S. Gu, and B. Poole, "Categorical reparameterization with gumbel-softmax," *arXiv preprint arXiv:1611.01144*, 2016.
- [61] N. Carion, F. Massa, G. Synnaeve, N. Usunier, A. Kirillov, and S. Zagoruyko, "End-to-end object detection with transformers," in *European conference on computer vision*. Springer, 2020, pp. 213–229.
- [62] X. Zhu, W. Su, L. Lu, B. Li, X. Wang, and J. Dai, "Deformable detr: Deformable transformers for end-to-end object detection," *arXiv preprint arXiv:2010.04159*, 2020.
- [63] H. Zhang, F. Li, S. Liu, L. Zhang, H. Su, J. Zhu, L. M. Ni, and H.-Y. Shum, "Dino: Detr with improved denoising anchor boxes for end-to-end object detection," *arXiv preprint arXiv:2203.03605*, 2022.
- [64] Y. Wang, V. C. Guizilini, T. Zhang, Y. Wang, H. Zhao, and J. Solomon, "Detr3d: 3d object detection from multi-view images via 3d-to-2d queries," in *Conference on Robot Learning*. PMLR, 2022, pp. 180–191.
- [65] R. Zhang, H. Qiu, T. Wang, Z. Guo, Z. Cui, Y. Qiao, H. Li, and P. Gao, "Monodetr: Depth-guided transformer for monocular 3d object detection," in *Proceedings of the IEEE/CVF International Conference on Computer Vision*, 2023, pp. 9155–9166.
- [66] Y. Zhou, H. Zhu, Q. Liu, S. Chang, and M. Guo, "Monoatt: Online monocular 3d object detection with adaptive token transformer," in *Proceedings of the IEEE/CVF Conference on Computer Vision and Pattern Recognition*, 2023, pp. 17 493–17 503.
- [67] C. Szegedy, S. Ioffe, V. Vanhoucke, and A. Alemi, "Inception-v4, inception-resnet and the impact of residual connections on learning," in *Proceedings of the AAAI conference on artificial intelligence*, vol. 31, no. 1, 2017.
- [68] X. Ding, X. Zhang, N. Ma, J. Han, G. Ding, and J. Sun, "Repvgg: Making vgg-style convnets great again," in *Proceedings of the IEEE/CVF conference on computer vision and pattern recognition*, 2021, pp. 13 733–13 742.
- [69] L. Yang, R.-Y. Zhang, L. Li, and X. Xie, "Simam: A simple, parameter-free attention module for convolutional neural networks," in *International conference on machine learning*. PMLR, 2021, pp. 11 863–11 874.
- [70] X. Li, W. Sun, and T. Wu, "Attentive normalization," in *Computer Vision—ECCV 2020: 16th European Conference, Glasgow, UK, August 23–28, 2020, Proceedings, Part XVII 16*. Springer, 2020, pp. 70–87.
- [71] H. Law and J. Deng, "Cornersnet: Detecting objects as paired keypoints," in *Proceedings of the European conference on computer vision (ECCV)*, 2018, pp. 734–750.
- [72] A. Mousavian, D. Anguelov, J. Flynn, and J. Kosecka, "3d bounding box estimation using deep learning and geometry," in *Proceedings of the IEEE conference on Computer Vision and Pattern Recognition*, 2017, pp. 7074–7082.
- [73] X. Chen, K. Kundu, Y. Zhu, A. G. Berneshawi, H. Ma, S. Fidler, and R. Urtasun, "3d object proposals for accurate object class detection," *Advances in neural information processing systems*, vol. 28, 2015.
- [74] D. P. Kingma, "Adam: A method for stochastic optimization," *arXiv preprint arXiv:1412.6980*, 2014.
- [75] Z. Wu, Y. Gan, Y. Wu, R. Wang, X. Wang, and J. Pu, "Fd3d: Exploiting foreground depth map for feature-supervised monocular 3d object detection," in *Proceedings of the AAAI Conference on Artificial Intelligence*, vol. 38, no. 6, 2024, pp. 6189–6197.
- [76] Y. Hu, S. Fang, W. Xie, and S. Chen, "Aerial monocular 3d object detection," *IEEE Robotics and Automation Letters*, vol. 8, no. 4, pp. 1959–1966, 2023.
- [77] L. Wang, L. Zhang, Y. Zhu, Z. Zhang, T. He, M. Li, and X. Xue, "Progressive coordinate transforms for monocular 3d object detection," *Advances in Neural Information Processing Systems*, vol. 34, pp. 13 364–13 377, 2021.
- [78] X. Shi, Z. Chen, and T.-K. Kim, "Multivariate probabilistic monocular 3d object detection," in *Proceedings of the IEEE/CVF winter conference on applications of computer vision*, 2023, pp. 4281–4290.